Hyperspectral Target Detection With Target Prior Augmentation and Background Suppression-Based Multidetector Fusion

Tan Guo, *Member, IEEE*, Fulin Luo, *Senior Member, IEEE*, Jiakun Guo, Yule Duan, Xinjian Huang, and Guangyao Shi

***Abstract*—Hyperspectral target detection (HTD) methods aim to exploit the abundant hyperspectral information to distinguish the key target pixels from multifarious background pixels. However, the performances of existing HTD methods are limited by the dilemmas of scarcity of target prior spectra, imprecise estimation of background spectra, as well as noise pollution. For the issues, this article proposes a novel target prior augmentation and background suppression-based multidetector fusion (TBMF) method for HTD, based on the joint optimization of the target prior spectra augmentation, low-rank pure background spectra separation, and nontarget nonbackground noise component removal. Specifically, a constrained linear spectral mixture model is seamlessly incorporated to implicitly augment the target's prior spectra. Also, the nontarget nonbackground components of HSI, i.e., noise with complex distribution are removed by a noise-robust $l_{1,1}$-norm-based regularization. Subsequently, multiple basic constrained energy minimization detectors are trained using the augmented diverse target spectra in the background-suppression subspace derived by the separated background spectra. The detection results of these basic detectors are fused with a winner-take-all strategy to acquire the final detection result. Plenty of experimental results on four HSI datasets show that the proposed TBMF method performs promisingly when compared with several classical and recently proposed HTD methods.**

***Index Terms*—Hyperspectral target detection (HTD), linear spectral mixture model, matrix decomposition, noise modeling.**

Manuscript received 29 August 2023; revised 27 September 2023 and 7 November 2023; accepted 4 December 2023. Date of publication 8 December 2023; date of current version 22 December 2023. This work was supported in part by the National Natural Science Foundation of China under Grant 62201109, Grant 62371076, Grant 62071340, and Grant 42201371, in part by the Key Scientific and Technological Innovation Project for "Chengdu-Chongqing Double City Economic Circle" under Grant KJCXZD2020025, and in part by the Open Project of Center for Applied Mathematics of Jiangsu Province (Nanjing University of Information Science and Technology). *(Corresponding author: Fulin Luo.)*

Tan Guo is with the School of Communication and Information Engineering, Chongqing University of Posts and Telecommunications, Chongqing 400065, China, and also with the Center for Applied Mathematics of Jiangsu Province, Nanjing University of Information Science and Technology, Nanjing 210044, China (e-mail: guot@cqupt.edu.cn).

Fulin Luo is with the School of Computer Science, Chongqing University, Chongqing 400044, China (e-mail: luoflyn@163.com).

Jiakun Guo is with the School of Communication and Information Engineering, Chongqing University of Posts and Telecommunications, Chongqing 400065, China (e-mail: 540641116@qq.com).

Yule Duan is with the College of Information Science and Engineering, Henan University of Technology, Zhengzhou 453000, China (e-mail: duanyule@haut.edu.cn).

Xinjian Huang is with the School of Cyber Science and Engineering, Nanjing University of Science and Technology, Nanjing 210094, China (e-mail: huangxinjian@njust.edu.cn).

Guangyao Shi is with the College of Computer Science and Technology, Chongqing University of Posts and Telecommunications, Chongqing 400065, China (e-mail: shigy@cqupt.edu.cn).

Digital Object Identifier 10.1109/JSTARS.2023.3340926

I. Introduction

THE hyperspectral spectrometer can simultaneously measure and record the electromagnetic energy scattering of land-cover objects in dozens or even hundreds of approximately continuous spectral bands [1], [2], [3], [32], [33], [34], [39], [40], [41]. As a result, the characteristic of high spectral resolution has enabled HSI to effectively identify different kinds of materials through precise spectral analysis, which has promoted a series of applications based on hyperspectral imaging [4], [5]. Among them, hyperspectral target detection (HTD) has attracted wide attention and shown great potential in both military and civilian fields, such as mineral resource exploration, military target survey, and object searching [6], [7], [8].

The basic task of HTD is to label each HSI test pixel as background or target and distinguish a small number of critical target pixels in HSI with the supervision of preacquired target prior spectra [9]. Many HTD methods have been proposed to address this challenging task and have achieved significant advances, such as the adaptive coherence estimator (ACE) [10], spectral angle mapper [11], adaptive subspace detector [12], and orthogonal subspace projection detector [13]. The existing methods usually construct detectors with the principles of suppressing the nontarget background spectra or highlighting the potential target spectra. For example, the constrained energy minimization (CEM) [14] and target-constrained interference minimization filter [15] impose constraints on the target or nontarget interference components and then construct a detector to highlight the target component by restricting the detector responses for background or nontarget interference components in HSI. Nevertheless, without accurate and sufficient background and target prior spectra, these methods cannot achieve reliable and satisfactory performance. In practice, obtaining adequate high-quality background and target prior spectra for HTD is labor-intensive or even impossible [16], [17].

Meanwhile, due to atmospheric interference, sensor noise, limited spatial resolution, and some other constraints during hyperspectral imaging, HSI pixels with blending and noise

pollution are ubiquitous, which has brought great difficulties for the accurate detection of target pixels [18]. In addition to this, the real-world target pixels for remote detection are usually different from the target prior spectra previously acquired using a handheld spectrometer in the laboratory or in the wild [19]. The handheld spectrometer is always very close to the surface of the target object rather than through remote sensing. Obviously, in a real HTD task, there is a data characteristic difference between the target spectra to be detected and the preacquired target prior spectra, which will increase the error probability for target spectra detection.

The root of the above problem lies in the variability of spectra, i.e., the same substance might show many differences in spectral characteristics. To alleviate the problem, one effective solution is the sparse representation-based target detection (SRD) method [20], by learning a sparse representation coefficient vector of a test pixel on a background and target union dictionary, and the detection of a target pixel is conducted by comparing the representation residuals. The main idea of SRD stems from linear subspace theory, with the underlying assumption that the spectra from background and target classes lie in different subspaces. Thus, target and background spectra can be separated by accurately constructing target and background spectral subspaces. The subspace models can produce diverse spectra through the linear combinations of limited preacquired target and the background prior spectra and, thus, have shown good efficiency in dealing with the spectral variability problem in HTD.

Therefore, SRD has triggered many representation-learning-based methods, such as the sparsity representation-based binary hypothesis (SRBBH) detector [21], binary-class collaborative representation-based detector [20], combined sparse and collaborative representation detector [22], and the sparse and dense hybrid representation-based target detector [23]. However, these representation-based HTD methods are extremely dependent on a pure and accurate estimation of background spectra dictionary, and the frequently used local dual concentric window strategy for background dictionary construction is cumbersome and subject to window parameters [21]. Thus, increasing efforts have been devoted to constructing or learning a unified background spectra dictionary. For example, Zhu et al. [17] proposed to construct a global overcomplete background spectra dictionary by using a classification-based background pixel selection strategy. Bitar et al. [19] proposed to directly learn a low-rank background dictionary from the observed HSI with the constraints of limited target prior spectra. However, these methods suffer from the problem of insufficient target prior spectra and are vulnerable to complex real-world noise interference, which will make the basic model assumptions no longer valid. As a result, the detection results of these methods will become unreliable.

In addition to the above shallow learning-based methods, some hierarchical learning-based methods have also been investigated for HSI applications [24], [25], [26], [35], [36], [37], [38]. For example, Gao et al. [38] proposed the depthwise feature interaction network with a depthwise cross-attention module to extract self-correlation and cross correlation from multisource feature pairs. Zou and Shi [24] proposed a multilayer hierarchical CEM (hCEM) detector by suppressing the undesired background spectra and preserving target spectra through a layer-by-layer filtering procedure. Zhu et al. [25] introduced a two-stream convolutional neural network-based target detector. However, the above-mentioned existing methods paid more attention to the discrimination and separability of target and background spectral components. However, HTD is not a naïve binary classification problem, and an ideal HSI target detector's function is beyond classification and should go further, that is, to highlight the target component and simultaneously suppress the background component. Furthermore, the imbalance in the number of the two classes of background and target prior spectra is also a key factor affecting detection performance.

Based on the above analysis, the dilemmas for existing HTD methods can be boiled down to one point for solving, i.e., learning adequate and high-quality target and background prior spectral components, and then highlighting the target component and suppressing the background component to distinguish targets. Accordingly, as shown in Fig. 1, this article proposes to augment the limited target prior spectra, and simultaneously to guide the separation of pure background component through HSI data decomposition. Specifically, we propose to insert a restricted linear spectral mixture model into the HSI data decomposition model, and implicitly generate and augment the target prior spectra via linear combinations of the limited target prior spectra, to provide more supervision information for target and background components decomposition. In addition, an $l_{1,1}$-norm regularization based on l_1-norm is introduced for complex HSI noise removal and endows the proposed model with noise-robust property. The above-mentioned several subproblems can be simultaneously optimized for the target augmentation and background suppression-based multidetector fusion-based HTD. In summary, the main contributions and highlights of this article are listed as follows.

1) The key objectives of HTD, i.e., diverse target prior spectra augmentation, low-rank pure background spectra separation, as well as complex nontarget nonbackground noise removal are jointly formulated in a single novel HSI data decomposition model for each individual component optimization with variables grouping.
2) A constrained linear spectral mixture model is seamlessly embedded into the HSI data decomposition model to implicitly augment the target prior spectra via the combinations of the limited target prior spectra. In addition, a complex noise-robust $l_{1,1}$-norm-based regularization is introduced to model and remove nontarget nonbackground noise components in HSI.
3) A group of basic CEM detectors is trained to make full use of the augmented diverse target prior spectra in the background-suppression subspace derived by the separated pure background spectra. The detection results of all these detectors are fused by a winner-take-all max-pooling strategy for the final detection result.

In the following, Section II presents some related works. An elaboration of the proposed TBMF method is given in Section III. The experimental results are reported in Section IV. Section V concludes the article.

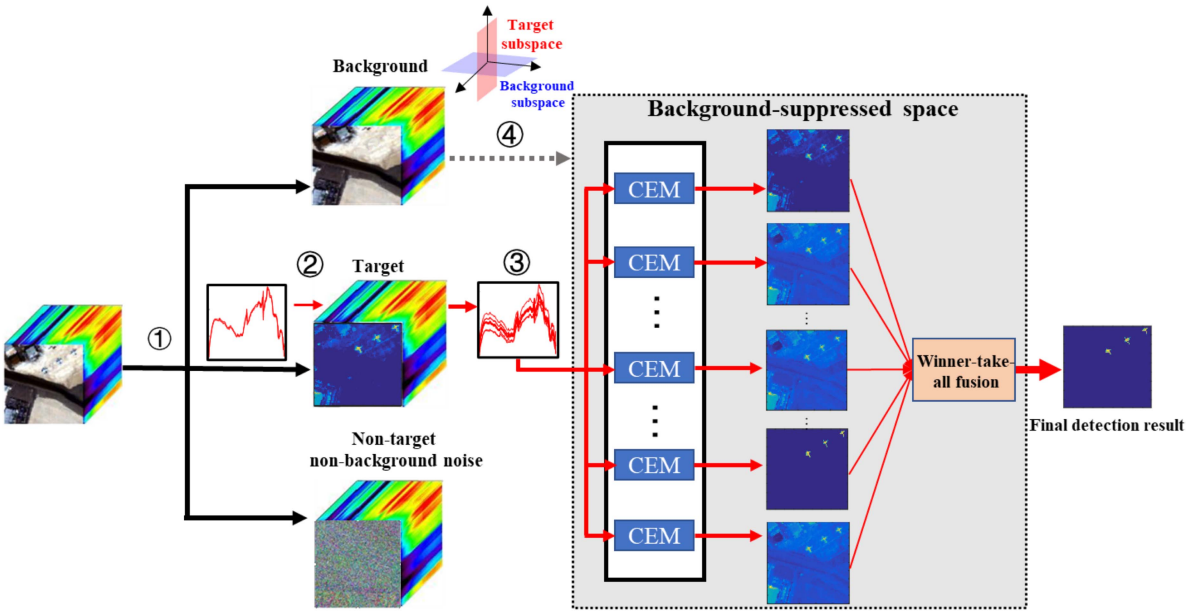

Fig. 1. Flowchart of the proposed TBMF method for HTD. ①HSI data decomposition model is established to pursue the augmentation-based target component, low-rank pure background component, and the nontarget nonbackground complex noise component. As shown in ② and ③, a constrained linear spectral mixture model is designed and embedded into the HSI decomposition procedure to simultaneously augment target prior spectra by linear combinations of limited target prior spectra. Through model optimization, the pure background component is separated to construct a background suppression subspace as in ④. The simultaneously obtained augmented target spectra are used to train multiple CEM detectors in the subspace, and the detection values from the CEM detector group are fused by a winner-take-all strategy for the final detection result.

II. Related Works

This section will introduce some relevant works to our proposed method for HTD, such as the low-rank learning methodologies and their applications for HTD.

A. Low-Rank Learning Methodology

The low-rank and low-dimensional characteristics of high-dimensional data are ubiquitous and usually follow the inherent physical mechanism of data generation. This is because many real-world data are an observation of some physical processes governed by certain generative mechanisms. For example, magnetic resonance images are generated by manipulating a magnetic field that obeys Maxwell's equations.

Due to the ubiquity and importance of low-rank structures, low-rank learning methodologies for high-dimensional data analysis are surging in popularity, such as robust principal component analysis (RPCA) [27] and low-rank representation (LRR) [28]. Specifically, RPCA considers how to recover the low-rank structure of a corrupted dataset when there is sparse noise with arbitrary magnitude. Considering a dataset $\mathbf{L} \in \Re^{d\times n}$ is corrupted by noise $\mathbf{E} \in \Re^{d\times n}$ that has the noised elements with arbitrary magnitude, and thus leads to a highly corrupted dataset $\mathbf{Y} \in \Re^{d\times n}$. The problem of recovering the original dataset $\mathbf{L}$ and its associated low-dimensional subspace from the highly corrupted observations $\mathbf{Y}$ is the so-called RPCA problem, i.e.,

$$\min_{\mathbf{L},\mathbf{E}} \text{rank}\,(\mathbf{L}) + \lambda\|\mathbf{E}\|_0 \text{ s.t. } \mathbf{Y} = \mathbf{L} + \mathbf{E} \tag{1}$$

where $\|\mathbf{E}\|_0$ indicates the number of the nonzero elements of the noise component $\mathbf{E}$. However, the RPCA model can only robustly extract a single subspace, that is, the linear subspace formed by all clean data. To solve the problem of clustering a set of data points that are sampled from a union of multiple low-dimensional subspaces with potential noise and corruptions, Liu et al. suggested the LRR model. Inspired by the sparse subspace clustering method [29], LRR promotes the representation coefficient matrix $\mathbf{Z}$ to be low rank by taking advantage of the self-expression property of data $\mathbf{Y}$. When considering possible sparse corruptions or outliers that are sampled outside of the subspaces, the LRR learning problem $\mathbf{Y} = \mathbf{YZ} + \mathbf{E}$ is solved with $\mathbf{E}$ being sparse or column-sparse, which leads to the following optimization formulation:

$$\min_{\mathbf{L},\mathbf{E}} \text{rank}\,(\mathbf{Z}) + \lambda\|\mathbf{E}\|_l \text{ s.t. } \mathbf{Y} = \mathbf{YZ} + \mathbf{E} \tag{2}$$

where $l = 0$ or $l = 2{,}0$ in $\|\mathbf{E}\|_l$, which means the noise in data is sparse or sample specific.

B. Low-Rank Modeling-Based HTD

The low-rank matrix recovery theory and methods have been applied and shown promising performance in the field of HSI processing, such as the HTD. For example, Bitar et al. [19] proposed a sparse and low-rank matrix decomposition method for automatic target Detection (SLRMDD) in hyperspectral imagery. Suppose an HSI is of the size of $h \times w \times p$, where h and w are the height and width of the image scene, respectively, and p is the number of the spectral bands. The HSI image is rearranged into a 2-D matrix $\mathbf{D}$, which is decomposed into a

low-rank matrix $\mathbf{A}$ as the pure background, a sparse matrix capturing any spatially small signals residing in the known target subspace spanned by the preacquired prior target spectra $\mathbf{S}$, and the noise, as follows:

$$\min_{\mathbf{A},\mathbf{X}} \|\mathbf{D}-\mathbf{A}-\mathbf{S}\mathbf{X}\|_F^2+\tau\|\mathbf{A}\|_*+\lambda\|\mathbf{X}\|_{2,1} \tag{3}$$

where the nuclear norm $\|\mathbf{A}\|_*$ is used as a surrogate for the matrix rank function $\text{rank}(\mathbf{A})$. The parameters τ and λ balance the contributions of the corresponding terms in the objective function. With the separated background component $\mathbf{A}$ and the target component $\mathbf{SX}$, the detection of target pixels is then performed by using the SRBBH scheme or using $\mathbf{SX}$ as the detector.

One of the key concerns for the model is the insufficient preacquired target prior spectra. If the available prior target spectra are limited, an accurate data decomposition cannot be guaranteed. In addition, the detection results will also be fragile to complex nontarget nonbackground interference noise.

III. Proposed Target Augmentation and Background Suppression-Based Multidetector Fusion for HSI Target Detection

A. Model Formulation

In an HTD task, the observed HSI dataset $\mathbf{D}\in\Re^{p\times N}$ is considered to contain three basic components, i.e., the background component $\mathbf{A}\in\Re^{p\times N}$, target component $\mathbf{T}\in\Re^{p\times N}$, and the nontarget nonbackground noise component $\mathbf{E}\in\Re^{p\times N}$. The three kinds of basic components mix to make up the final observed HSI data $\mathbf{D}$. Conversely, inferring the three components from the observed $\mathbf{D}$ with the guidance of preacquired target prior spectra $\mathbf{S}\in\Re^{p\times n_1}$ is regarded as an inversion problem through data decomposition, which is mathematically formulated as follows:

$$\min_{\mathbf{A},\mathbf{B},\mathbf{E}} \Phi(\mathbf{A})+\Psi(\mathbf{T},\mathbf{S})+\Omega(\mathbf{E}) \text{ s.t. } \mathbf{D}=\mathbf{A}+\mathbf{T}+\mathbf{E}. \tag{4}$$

Obviously, there are numerous solutions to the above problem, and without some prior knowledge and regularizations about the characteristics of the three HSI components, an accurate and meaningful data decomposition is unable to be obtained. Consequently, in the objective function of (4), $\Phi(\mathbf{A})$ contains some prior knowledge or constraint regularizations for background component $\mathbf{A}$. $\Psi(\mathbf{T},\mathbf{S})$ should be able to characterize the target component $\mathbf{T}$ in HSI, and the target component $\mathbf{T}$ must have a high similarity to the preacquired target prior spectra $\mathbf{S}$. At last, the nontarget nonbackground noise component $\mathbf{E}$ should be properly identified and handled with via $\Omega(\mathbf{E})$ to reduce its repercussions on the accurate decomposition of target and background components.

In real-world HSI data, a key observation is that the background pixels, which contain some different materials, are locally similar and with limited variability [19]. When unfolding the HSI data and lexicographically arranging the locally similar background pixels, it will be found that the pure background component should have a low-dimensional structure, which can be modeled using the low-rank constraint. However, when mixing with target and noise components, the rank of the background component will increase. In other words, the pure background component can be achieved by separating a rank-reduced component $\mathbf{A}$ from $\mathbf{D}$ as follows:

$$\min_{\mathbf{A},\mathbf{T},\mathbf{E}} \text{rank}(\mathbf{A})+\Psi(\mathbf{T},\mathbf{S})+\Omega(\mathbf{E}) \quad \text{s.t. } \mathbf{D}=\mathbf{A}+\mathbf{T}+\mathbf{E}. \tag{5}$$

It is known that in comparison to the background pixels, target pixels are small in number. As a result, the nonzero column supports of $\mathbf{T}$ are sparse and can roughly indicate the positions of the target pixels. In addition, the similarity between the target component $\mathbf{T}$ and preacquired target prior spectra $\mathbf{S}$ must be strengthened. In the end, one can choose to promote $\mathbf{T}=\mathbf{SX}$ with a learnable abundance matrix $\mathbf{X}$. The principle behind this is that the linear combinations of the preacquired target prior spectra $\mathbf{S}$ can be used to form the target component $\mathbf{T}$ of $\mathbf{D}$. However, the number of the preacquired target spectra $\mathbf{S}$ is always very limited, i.e., n_1 is usually very small, which might be unable to provide sufficient and diverse supervision knowledge for accurate data decomposition. Alternatively, we introduce a learnable target component dictionary $\mathbf{B}\in\Re^{p\times n_2}$ containing n_2 atoms to replace $\mathbf{S}$ with $n_2>n_1$. Thus, the number of target pixels in the data decomposition model (5) will be augmented from n_1 to n_2, which can provide more degrees of freedom for fitting the data decomposition model in comparison to directly using the original target prior spectra $\mathbf{S}$, resulting in the following model:

$$\min_{\mathbf{A},\mathbf{B},\mathbf{X},\mathbf{E}} \text{rank}(\mathbf{A})+\Psi(\mathbf{B},\mathbf{S},\mathbf{X})+\Omega(\mathbf{E}) \quad \text{s.t. } \mathbf{D}=\mathbf{A}+\mathbf{B}\mathbf{X}+\mathbf{E} \tag{6}$$

where $\Psi(\mathbf{B},\mathbf{S},\mathbf{X})$ is used to regulate the target component dictionary $\mathbf{B}$ and the column-spare target component $\mathbf{BX}$, with the guidance of preacquired target prior spectra $\mathbf{S}$. Since a column-sparse $\mathbf{X}$ can promote $\mathbf{BX}$ to be sparse in the column, the sparsity prior property of target component $\mathbf{BX}$ can be achieved by minimizing the nonzero column supports of $\mathbf{X}$, which can be modeled as the $l_{2,0}$-norm of $\mathbf{X}$, i.e., $\|\mathbf{X}\|_{2,0}=\#\{i:\|[\mathbf{X}]_{:,i}\|_2\neq 0\}$, and $[\mathbf{X}]_{:,i}$ is the ith column of $\mathbf{X}$. To incorporate the target prior spectra $\mathbf{S}$, we proposed to connect $\mathbf{B}$ and $\mathbf{S}$ via a constrained linear spectral mixture model as $\mathbf{B}=\mathbf{SC}$ with a sum-to-one constraint for the linear combination matrix $\mathbf{C}\in\Re^{n_1\times n_2}$, i.e., $\mathbf{C}^{\mathrm{T}}1_{n_1\times 1}=1_{n_2\times 1}$, and 1 is a column vector with all its value per dimension as 1, which can enhance the physical interpretability of the linear mixture model. Finally, the complex nontarget nonbackground noise component $\mathbf{E}$ is estimated using $\|\mathbf{E}\|_{1,0}=\#\{j:\|[\mathbf{E}]_{:,j}\|_1\neq 0\}$, and $[\mathbf{E}]_{:,j}$ is the jth column of $\mathbf{E}$. Accordingly, our target and background decomposition model is finally formulated as follows:

$$\min_{\mathbf{A},\mathbf{B},\mathbf{X},\mathbf{C},\mathbf{E}} \text{rank}(\mathbf{A})+\frac{\alpha}{2}\|\mathbf{B}-\mathbf{SC}\|_F^2+\beta\|\mathbf{X}\|_{2,0}+\gamma\|\mathbf{E}\|_{1,0} \quad \text{s.t. } \mathbf{D}=\mathbf{A}+\mathbf{B}\mathbf{X}+\mathbf{E},\ \mathbf{C}^{\mathrm{T}}1_{n_1\times 1}=1_{n_2\times 1}. \tag{7}$$

TABLE I
MAIN NOTATIONS AND THEIR MEANINGS USED IN THIS ARTICLE

Notation	Meaning	Notation	Meaning
$\mathbf{Y} \in \Re^{d\times n}$	A highly corrupted dataset	$\mathbf{A} \in \Re^{p\times N}$	Background component of HSI dataset $\mathbf{D}$
$\mathbf{L} \in \Re^{d\times n}$	Low-rank component of dataset $\mathbf{Y}$	$\mathbf{T} \in \Re^{p\times N}$	Target component of HSI dataset $\mathbf{D}$
$\mathbf{N} \in \Re^{d\times n}$	Noise component of dataset $\mathbf{Y}$	$\mathbf{S} \in \Re^{p\times n_1}$	Pre-acquired target prior spectra
$\mathbf{Z} \in \Re^{n\times n}$	LRR matrix of $\mathbf{Y}$	$\mathbf{B} \in \Re^{p\times n_2}$	Target component dictionary
$\mathbf{D} \in \Re^{p\times N}$	Observed HSI dataset	$\mathbf{C} \in \Re^{n_1\times n_2}$	Linear combination matrix of $\mathbf{B}$ on $\mathbf{S}$
$\mathbf{E} \in \Re^{p\times N}$	Noise component of HSI dataset $\mathbf{D}$	$\mathbf{X} \in \Re^{n_2\times N}$	Target component abundance matrix in HSI dataset $\mathbf{D}$

The above-mentioned data decomposition problem is generally NP-hard because of the existence of the matrix rank function $\text{rank}(\cdot)$ and l_0-norm. Fortunately, it is feasible and efficient to use the nuclear norm as a surrogate for the matrix rank function in (7). Also, $l_{2,1}$ and $l_{1,1}$ norms are applicable relaxations for $l_{2,0}$ and $l_{1,0}$ regularization norms, respectively. Therefore, the proposed model is transformed into the following relaxed optimization problem:

$$\min_{\mathbf{A},\mathbf{B},\mathbf{X},\mathbf{C},\mathbf{E}} \|\mathbf{A}\|_* + \frac{\alpha}{2}\|\mathbf{B}-\mathbf{SC}\|_F^2 + \beta\|\mathbf{X}\|_{2,1} + \gamma\|\mathbf{E}\|_{1,1}$$
$$\text{s.t. } \mathbf{D} = \mathbf{A} + \mathbf{BX} + \mathbf{E},\ \mathbf{C}^{\mathrm{T}}\, 1_{n_1\times 1} = 1_{n_2\times 1}. \tag{8}$$

The main notations and their meanings used in the article are summarized in Table I. In summary, the proposed model focuses on the three important problems in HTD, i.e., pure background component separation, diverse target prior spectra augmentation, as well as the complex nontarget nonbackground noise component estimation and removal. The three objectives affect each other and a satisfactory solution can be achieved via proper and efficient optimization.

B. Model Optimization

There are five variables in the HSI data decomposition model (8), which is a multiple-variable optimization problem involving three subproblems, including: 1) target spectra augmentation (TSA); 2) target spectra abundance optimization (TSAO); and 3) background spectra optimization (BSO). Therefore, the original optimization problem is divided into three subproblems for solving with variables grouping, including the TSA subproblem for optimizing $\mathbf{B}$, $\mathbf{C}$, and $\mathbf{E}$ with the other variables fixed, the TSAO subproblem for optimizing $\mathbf{X}$ and $\mathbf{E}$ by fixing the other variables, and the BSO subproblem for optimizing $\mathbf{A}$ and $\mathbf{E}$ with the other variables frozen. The details for solving these subproblems are presented as follows.

1) TSA Subproblem Optimization: In this optimization problem, variables $\mathbf{A}$ and $\mathbf{X}$ are fixed to optimize $\mathbf{B}$, $\mathbf{C}$, and $\mathbf{E}$, which results in the following problem:

$$\min_{\mathbf{B},\mathbf{C},\mathbf{E}} \frac{\alpha}{2}\|\mathbf{B}-\mathbf{SC}\|_F^2 + \gamma\|\mathbf{E}\|_{1,1}$$
$$\text{s.t. } \mathbf{D}-\mathbf{A} = \mathbf{BX}+\mathbf{E},\ \mathbf{C}^{\mathrm{T}}\, 1_{n_1\times 1} = 1_{n_2\times 1}. \tag{9}$$

This can be solved by the augmented Lagrange multiplier (ALM) method [30] that converts (9) into the following minimized equivalent problem:

$$\min_{\mathbf{B},\mathbf{C},\mathbf{E}} \frac{\alpha}{2}\|\mathbf{B}-\mathbf{SC}\|_F^2 + \gamma\|\mathbf{E}\|_{1,1} + \frac{\mu}{2}\|\mathbf{D}-\mathbf{A}-\mathbf{BX}-\mathbf{E}\|_F^2$$
$$+ \langle \mathbf{Y}_1, \mathbf{D}-\mathbf{A}-\mathbf{BX}-\mathbf{E}\rangle$$
$$\text{s.t. } \mathbf{C}^{\mathrm{T}}\, 1_{n_1\times 1} = 1_{n_2\times 1} \tag{10}$$

where $\langle \mathbf{P}, \mathbf{Q}\rangle = \text{trace}(\mathbf{P}^{\mathrm{T}}\mathbf{Q})$. $\mathbf{Y}_1$ is the Lagrange multiplier and μ is a penalty parameter. Algorithm 1 summarizes the solution to problem (9) and step 2 is solved via the soft-threshold operation.

2) TSAO Subproblem Optimization: Afterward, the TSAO subproblem will be handled, i.e., optimizing variables $\mathbf{X}$ and $\mathbf{E}$ by fixing the others as follows:

$$\min_{\mathbf{X},\mathbf{E}} \beta\|\mathbf{X}\|_{2,1} + \gamma\|\mathbf{E}\|_{1,1}$$
$$\text{s.t. } \mathbf{D}-\mathbf{A} = \mathbf{BX}+\mathbf{E}. \tag{11}$$

To make the problem (11) more tractable, an auxiliary variable $\mathbf{J}$ is introduced to convert (11) into the following equivalent optimization problem:

$$\min_{\mathbf{X},\mathbf{E},\mathbf{J}} \beta\|\mathbf{J}\|_{2,1} + \gamma\|\mathbf{E}\|_{1,1}$$
$$\text{s.t. } \mathbf{D}-\mathbf{A} = \mathbf{BX}+\mathbf{E},\ \mathbf{X} = \mathbf{J}. \tag{12}$$

Again, the ALM method is applied to covert (12) into an unconstrained minimization optimization problem as follows

$$\min_{\mathbf{X},\mathbf{E},\mathbf{J}} \beta\|\mathbf{J}\|_{2,1} + \gamma\|\mathbf{E}\|_{1,1} + \frac{\mu}{2}\|\mathbf{D}-\mathbf{A}-\mathbf{BX}-\mathbf{E}\|_F^2$$
$$+ \langle \mathbf{Y}_2, \mathbf{D}-\mathbf{A}-\mathbf{BX}-\mathbf{E}\rangle + \frac{\mu}{2}\|\mathbf{X}-\mathbf{J}\|_F^2 + \langle \mathbf{Y}_3, \mathbf{X}-\mathbf{J}\rangle \tag{13}$$

where $\mathbf{Y}_2$ and $\mathbf{Y}_3$ are the Lagrange multipliers and μ a penalty parameter. The inexact ALM method to solve (11) is outlined in Algorithm 2, of which steps 2 and 3 are solved by the soft-threshold operation.

3) BSO Subproblem Optimization: With the optimized $\mathbf{B}$ and $\mathbf{X}$ fixed, the last step is to optimize the variables $\mathbf{A}$ and $\mathbf{E}$, i.e., solving the BSO subproblem as follows:

$$\min_{\mathbf{A},\mathbf{E}} \|\mathbf{A}\|_* + \gamma\|\mathbf{E}\|_{1,1}$$
$$\text{s.t. } \mathbf{D}-\mathbf{BX} = \mathbf{A}+\mathbf{E}. \tag{14}$$

Algorithm 1: Solving TSA Subproblem (9) by Inexact ALM.

Input: $\mathbf{D}$, $\mathbf{A}$, $\mathbf{X}$, and parameters α and γ.
Initialize: $\mathbf{B} = \mathbf{J} = 0, \mathbf{E} = 0, \mathbf{Y}_1 = \mathbf{0}, \mathbf{Y}_2 = 0, \mu = 10^{-3}, \mu_{\max} = 10^6, \rho = 1.5, \theta = 10^{-6}$.
While *not converged* **do**
1. Fix the other variables and update $\mathbf{B}$ via
$\mathbf{B} = (\alpha\mathbf{SC} + \mu(\mathbf{D} - \mathbf{A} - \mathbf{E} + \mathbf{Y}_1/\mu)\mathbf{X}^T)\,(\alpha\mathbf{I} + \mu\mathbf{X}\mathbf{X}^T)^{-1}$
2. Fix the other variables and update $\mathbf{E}$ via
$\frac{\gamma}{\mu}\|\mathbf{E}\|_{1,1} + \frac{1}{2}\|\mathbf{E} - (\mathbf{D} - \mathbf{A} - \mathbf{BX} + \mathbf{Y}_1/\mu)\|_F^2$
3. Fix the other variables and update $\mathbf{C}$ via
$\mathbf{C} = \alpha(\alpha\mathbf{S}^T\mathbf{S} + 2\mathbf{I})^{-1}\mathbf{S}^T\mathbf{B}$ with $\mathbf{C}^{\mathrm{T}}\, 1_{n_1\times 1} = 1_{n_2\times 1}$
4. Update μ by $\mu = \min(\rho\mu,\ \mu_{\max})$
5. Check the convergence condition: $\|\mathbf{D} - \mathbf{A} - \mathbf{BX} - \mathbf{E}\|_F^2 < \theta$
end
Output: $\mathbf{B}$ and $\mathbf{C}$

Algorithm 2: Solving TSAO Subproblem (11) by Inexact ALM.

Input: $\mathbf{D}$, $\mathbf{A}$, $\mathbf{B}$, and parameters β and γ.
Initialize: $\mathbf{X} = \mathbf{E} = \mathbf{0}, \mathbf{Y}_2 = \mathbf{0}, \mathbf{Y}_3 = \mathbf{0}, \eta = 10^{-3}, \eta_{\max} = 10^6, \rho = 1.5, \theta = 10^{-6}$.
While *not converged* **do**
1. fix the others and update $\mathbf{X}$ via
$\mathbf{X} = (\mathbf{B}^T\mathbf{B} + \mathbf{I})^{-1}\,(\mathbf{B}^T(\mathbf{D} - \mathbf{A} - \mathbf{E} + \mathbf{Y}_2/\eta) + \mathbf{J} - \mathbf{Y}_3/\eta)$
2. fix the others and update $\mathbf{E}$ via
$\mathbf{E} = \arg\min_{\mathbf{E}} \frac{\gamma}{\eta}\|\mathbf{E}\|_{1,1} + \frac{1}{2}\|\mathbf{E} - (\mathbf{D} - \mathbf{A} - \mathbf{BX} + \mathbf{Y}_2/\eta)\|_F^2$
3. fix the others and update $\mathbf{J}$ via
$\mathbf{J} = \arg\min_{\mathbf{J}} \frac{\beta}{\eta}\|\mathbf{J}\|_{2,1} + \frac{1}{2}\|\mathbf{J} - (\mathbf{X} + \mathbf{Y}_3/\eta)\|_F^2$
4. update penalty parameter η by $\eta = \min(\rho\eta,\ \eta_{\max})$
5. check the convergence conditions: $\|\mathbf{D} - \mathbf{A} - \mathbf{BX} - \mathbf{E}\|_F^2 < \theta$ and $\|\mathbf{X} - \mathbf{J}\|_F^2 < \theta$
end
Output: $\mathbf{X}$.

Algorithm 3: Solving BSO Subproblem (14) by Inexact ALM.

Input: $\mathbf{D}$, $\mathbf{A}$, $\mathbf{B}$, $\mathbf{C}$, and the parameters β and γ.
Initialize: $\mathbf{X} = \mathbf{E} = 0, \mathbf{Y}_4 = \mathbf{0}, \zeta = 10^{-3}, \zeta_{\max} = 10^6, \rho = 1.5, \theta = 10^{-6}$.
While *not converged* **do**
1. fix the others and update $\mathbf{A}$ via
$\mathbf{A} = \operatorname{argmin}_{\mathbf{A}} \|\mathbf{A}\|_* + \frac{\zeta}{2}\|\mathbf{D} - \mathbf{BX} - \mathbf{A} - \mathbf{E} + \mathbf{Y}_4/\zeta\|_F^2$
2. fix the others and update $\mathbf{E}$ via
$\mathbf{E} = \operatorname{argmin}_{\mathbf{E}} \gamma\|\mathbf{E}\|_{1,1} + \frac{\zeta}{2}\|\mathbf{D} - \mathbf{BX} - \mathbf{A} - \mathbf{E} + \mathbf{Y}_4/\zeta\|_F^2$
3. update ζ by $\zeta = \min(\rho\zeta,\ \zeta_{\max})$
4. check the convergence condition: $\|\mathbf{D} - \mathbf{A} - \mathbf{BX} - \mathbf{E}\|_F^2 < \theta$
end
Output: $\mathbf{A}$.

Similarly, the ALM scheme is applied to covert (14) into an unconstrained minimization problem as follows:

$$\min_{\mathbf{A},\mathbf{E}} \|\mathbf{A}\|_* + \gamma\|\mathbf{E}\|_{1,1} + \frac{\zeta}{2}\|\mathbf{D} - \mathbf{BX} - \mathbf{A} - \mathbf{E}\|_F^2 + \langle \mathbf{Y}_4, \mathbf{D} - \mathbf{BX} - \mathbf{A} - \mathbf{E}\rangle \tag{15}$$

where ζ is a penalty parameter and $\mathbf{Y}_4$ is the Lagrange multiplier matrix. The procedures for solving (14) are presented in Algorithm 3, wherein steps 1 and 2 both have closed-form solutions [29], [30].

C. Target Detection by Fusing Multiple CEM Detectors

After solving the optimization Algorithms 1–3, the pure background component $\mathbf{A} \in \Re^{p\times N}$ and augmented diverse target component $\mathbf{B} = [\boldsymbol{b}_1, \boldsymbol{b}_2, \ldots, \boldsymbol{b}_{n_2}] \in \Re^{p\times n_2}$ will be obtained. To enhance the discrimination and separation between the target

Algorithm 4: Proposed Target Augmentation and Background Suppression-Based Multidetector Fusion for HTD.

Input: HSI dataset $\mathbf{D}$ and target prior spectra $\mathbf{S}$. The parameters α, β, and γ. Iteration number *In*.
Initialize: $\mathbf{X}$ and $\mathbf{C}$. SVD of $\mathbf{D} = \mathbf{U}\mathbf{\Sigma}\mathbf{V}^{\mathrm{T}}$, $\mathbf{A} = \mathbf{U}(:, 1:10) * \mathbf{\Sigma}(1:10, 1:10) * \mathbf{V}(:, 1:10)'$.
1. for 1: *In* **do**
I. solving TSA subproblem using Algorithm 1.
II. solving TSAO subproblem using Algorithm 2.
III. solving BSO subproblem using Algorithm 3.
end
2. utilize the optimized background component $\mathbf{A}$ to construct a background-suppressed space as in (16).
3. transform the target component $\mathbf{B}$ into the background-suppressed space to get the background-suppressed target component $\mathbf{B}^{bs}$ and HSI data $\mathbf{D}^{bs}$.
4. train multiple CEM target detectors using $\mathbf{B}^{bs}$, and fuse the multiple detection maps via winner-take-all to get the final detection map.
Output: Detection map.

and background components, an orthogonal complement subspace is constructed based on $\mathbf{A}$ as follows:

$$\mathbb{S}_{\mathbf{A}}^{\perp} = \mathbf{I} - \mathbf{A}\left(\mathbf{A}^{\mathrm{T}}\mathbf{A}\right)^{-1}\mathbf{A}^{\mathrm{T}}. \tag{16}$$

The subspace spanned by $\mathbb{S}_{\mathbf{A}}^{\perp}$ is orthogonal to the background component subspace, and thus constitutes a background-suppression subspace, wherein the background component is suppressed and the nonbackground components, such as the target component and nontarget nonbackground noise interference component can be relatively highlighted.

After that, the target component $\mathbf{B}$ and noise removed HSI data $\mathbf{D}_{nr} = \mathbf{D} - \mathbf{E}$ are projected into the background-suppressed space, obtaining the corresponding background-suppressed target and background mixed components, i.e., $\mathbf{B}^{bs} = \mathbb{S}_{\mathbf{A}}^{\perp}\,\mathbf{B} = [\mathbf{b}_1^{bs}, \mathbf{b}_2^{bs}, \ldots, \mathbf{b}_{n_2}^{bs},] \in \Re^{p\times n_2}$ and $\mathbf{D}_{nr}^{bs} = \mathbb{S}_{\mathbf{A}}^{\perp}\,\mathbf{D}_{nr} = [\mathbf{d}_{nr\cdot 1}^{bs}, \mathbf{d}_{nr\cdot 2}^{bs}, \ldots, \mathbf{d}_{nr\cdot N}^{bs}] \in \Re^{p\times N}$. The background-suppressed target components $\mathbf{B}^{bs}$ with n_2 diverse target spectra are then utilized for training n_2 CEM detectors, and the filter for the ith CEM detector is established as follows:

$$\mathbf{w}_i = \left(\mathbf{R}^{-1}\mathbf{b}_i^{bs}\right) / \left(\left(\mathbf{b}_i^{bs}\right)^{T}\mathbf{R}^{-1}\left(\mathbf{b}_i^{bs}\right)\right) \tag{17}$$

where $\mathbf{R} = \left(\sum_{j=1}^{N}(\mathbf{d}_{nr\cdot j}^{bs})(\mathbf{d}_{nr\cdot j}^{bs})^{T}\right)/N$ is the covariance matrix for the background-suppressed HSI data $\mathbf{D}_{nr}^{bs}$. The obtained n_2 CEM detectors are then utilized for detecting the targets in the background-suppressed HSI data $\mathbf{D}_{nr}^{bs}$, with each CEM detector producing one detection map. Afterward, the winner-take-all max-pooling fusion operation is performed to acquire the final detection result as follows:

$$\mathrm{DetecMap} = \mathrm{MaxPool}\left\{\mathbf{w}_i\mathbf{D}_{nr}^{bs}\right\}_{i=1}^{n_2}. \tag{18}$$

The operation makes full use of the enhanced diverse target spectra, which can lead to a robust detection result. The whole procedures for our HTD method are outlined in Algorithm 4.

D. Algorithm Complexity Analysis

In Algorithm 1, the main computational complexity lies in steps 1 and 3, which involve matrix inversion and matrix multiplications. In step 1 of Algorithm 1, $(\alpha\mathbf{I} + \mu\mathbf{X}\mathbf{X}^{T})^{-1}$ costs $\mathcal{O}(Nn_2^2 + n_2^3)$ and can be precalculated and cached. In step 3 of Algorithm 1, $(\alpha\mathbf{S}^{T}\mathbf{S} + 2\mathbf{I})^{-1}$ is computed and cached at the cost of $\mathcal{O}(pn_1^2 + n_1^3)$. The main computational complexity of Algorithm 1 is $\mathcal{O}(Nn_2^2 + n_2^3 + pn_1^2 + n_1^3 + \rho(pn_2^2 + pn_1^2 + pn_1n_2))$, where ρ is the iteration number. Similarly, the main computational complexity of Algorithm 2 lies in step 1, whose matrix inversion and matrix multiplications cost $\mathcal{O}(pn_2^2 + n_2^3 + \omega(Nn_2^2 + pNn_2))$ with ω iterations. The singular value decomposition (SVD) in step 1 of Algorithm 3 costs $\mathcal{O}(N^3)$. The computation complexity Algorithm 4 mainly comes from Algorithms 1–3, with a factor of iteration number *In*. Step 2 involves matrix multiplication and inversion, the total computation complexity of which is $\mathcal{O}(N^3 + N^2p)$.

In addition, the convergence property of inexact ALM has been proved [28], and the performance and convergence curves of our algorithm shown in Section VI provide evidence that the devised algorithms converge quickly in practice.

IV. Experimental Results

A. Experimental Setup

The first three datasets used in the experiments are denoted as AVIRIS I, AVIRIS II, and AVIRIS III, which are collected by the airborne visible/infrared imaging spectrometer (AVIRIS) from San Diego with a spatial resolution of 3.5 m. The low signal-to-noise ratio, water absorption, and some bad bands are removed. A total of 189 bands were remained for experiments [24]. The three datasets and their corresponding ground-truths are shown in Figs. 2–4, which have 60 × 60 pixels, 100 × 100 pixels, and 100 × 100 pixels, respectively. In Fig. 2(b), there are 14 airplanes containing 119 pixels to detect in the AVIRIS I dataset. For the AVIRIS II dataset, the airplanes with special spectral characteristics were selected as the targets to detect, which have 58 pixels, as shown in Fig. 3(b). In the AVIRIS III dataset, there are 134 pixels distributed in planes for detection, as demonstrated in Fig. 4(b).

The fourth benchmark data are collected in an HSI data collection campaign called "Viareggio 2013 trial" [17]. The datasets in the campaign are assembled via a push-broom sensor termed "Sistema Iperspettrale Modulare Galileo Avionica." In the datasets, the D1F12H1 is used in the experiment, and the subset has 375 × 450 pixels and covers a parking lot, a football

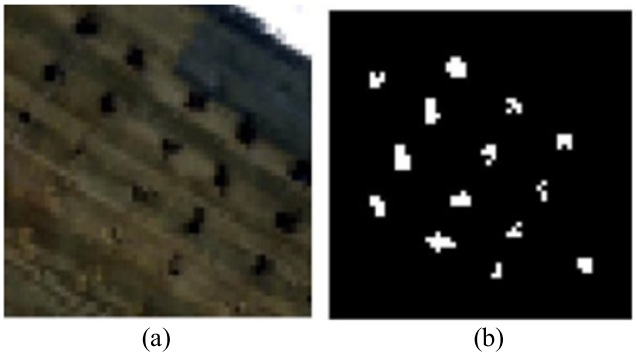

Fig. 2. AVIRIS I hyperspectral data. (a) Image scene. (b) Ground-truth.

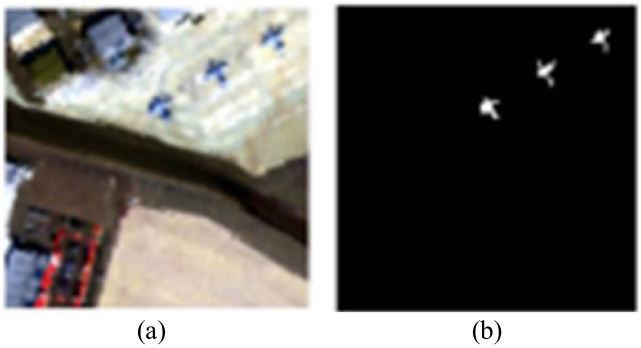

Fig. 3. AVIRIS II hyperspectral data. (a) Image scene. (b) Ground-truth.

field, and several sports facility buildings, as shown in Fig. 5(a). The wavelength range of this dataset is 400–1000 nm and there are 511 spectral bands in total. The spatial resolution and spectral resolution are 0.6 m and 2.3 nm, respectively. A subscene, as shown in Fig. 5(b) with 100 × 100 pixels, is used. There are three panels containing 24 pixels that are regarded as targets for detection and the ground-truth is given in Fig. 5(c).

To evaluate the performance of different HTD methods, the probability of false alarm ($\mathrm{P}_{\mathrm{F}}^{\tau}$) and the probability of detection ($\mathrm{P}_{\mathrm{D}}^{\tau}$) under different thresholds τ are calculated as follows:

$$\mathrm{P}_{\mathrm{D}}^{(\tau)} = \frac{\mathrm{TP}^{(\tau)}}{\mathrm{N_t}} \tag{19}$$

$$\mathrm{P}_{\mathrm{F}}^{(\tau)} = \frac{\mathrm{FP}^{(\tau)}}{\mathrm{N_b}} \tag{20}$$

where $\mathrm{TP}^{(\tau)}$ and $\mathrm{FP}^{(\tau)}$ represent the number of targets and background pixels whose detection value is larger than the given threshold τ. $\mathrm{N_t}$ and $\mathrm{N_b}$ are the total numbers of true target and background pixels, respectively.

The receiver operating characteristic (ROC) curve can provide a threshold-free performance metric in terms of $\mathrm{P}_{\mathrm{F}}^{(\tau)}$ and $\mathrm{P}_{\mathrm{D}}^{(\tau)}$. Under the same $\mathrm{P}_{\mathrm{F}}^{(\tau)}$ level, a detector with higher $\mathrm{P}_{\mathrm{D}}^{(\tau)}$ is claimed to have better detection performance. In addition, the area under the curve (AUC) enclosed by the ROC curve and the coordinate axes is also widely employed as a quantitative index for detection performance evaluation.

However, an ROC curve of $(\mathrm{P}_{\mathrm{D}}^{(\tau)}, \mathrm{P}_{\mathrm{F}}^{(\tau)})$ under all possible threshold τ can only be used to evaluate the effectiveness of a detector but not its target detectability and background suppressibility. Both $\mathrm{P}_{\mathrm{D}}^{(\tau)}$ and $\mathrm{P}_{\mathrm{F}}^{(\tau)}$ are a function of the independent parameter specified by the threshold τ. On some occasions, two detectors yielding two different ROC curves indeed obtain the same AUC value in terms of $(\mathrm{P_D}, \mathrm{P_F})$. To alleviate the problem, the 3-D ROC curve is designed to include the threshold value as an independent variable [31] and then generates an ROC curve in a 3-D space of $(\mathrm{P_D}, \mathrm{P_F}, \tau)$. In addition to the 3-D ROC curve, three corresponding 2-D ROC curves, i.e., 2-D ROC curve of $(\tau, \mathrm{P_F})$, 2-D ROC curve of $(\tau, \mathrm{P_D})$, and 2-D ROC curve of $(\mathrm{P_F}, \mathrm{P_D})$, and the AUC of the three kinds of 2-D ROC curve are used to comprehensively evaluate the performance of different detectors [31]. As a result, an efficient detector should have a higher $\mathrm{AUC}_{(\mathrm{P_F},\mathrm{P_D})}$ and $\mathrm{AUC}_{(\tau,\ \mathrm{P_D})}$ when they approach 1, and meanwhile, a lower $\mathrm{AUC}_{(\tau,\ \mathrm{P_F})}$ approaching 0 will be preferred. Therefore, an overall AUC value is calculated by comprehensively considering $\mathrm{AUC}_{(\mathrm{P_F},\mathrm{P_D})}$, $\mathrm{AUC}_{(\mathrm{P_F},\mathrm{P_D})}$, and $\mathrm{AUC}_{(\tau,\ \mathrm{P_F})}$ for overall performance evaluation as follows:

$$\mathrm{AUC_{OA}} = \mathrm{AUC}_{(\mathrm{P_F},\mathrm{P_D})} + \mathrm{AUC}_{(\tau,\mathrm{P_D})} - \mathrm{AUC}_{(\tau,\mathrm{P_F})} \tag{21}$$

$$\mathrm{AUC_{SNPR}} = \mathrm{AUC}_{(\tau,\mathrm{P_D})}/\mathrm{AUC}_{(\tau,\mathrm{P_F})}. \tag{22}$$

B. Comparison Methods

In the experiments, several representative HTD methods have been selected for performance comparison, including ACE, CEM, SRD, hCEM, SLRMDD, and SSBRTD. Among them, ACE is a benchmark detector, which has been proved to be effective with a single prior target spectrum, and is taken as an example of the matched filter type detectors. The CEM detector achieves detection results by filtering technique, which is an effective method to highlight the targets in HSI. SRD utilizes the sparse representation theory to pursue a sparse representation of a test pixel on the background and target union dictionary, the calculated two representation residuals are compared for the final detection decision [20]. Through a layer-by-layer hierarchical filtering procedure, hCEM can hierarchically suppress the undesired background spectra and hold the main energy of target spectra [24]. SLRMDD can be seen as a modified RPCA model and can separate the known targets of interest from the background in hyperspectral imagery [19]. SSBSTD proposes to construct a target dictionary and an overcomplete background dictionary by the manners of target predetection and common pixels selection [17]. In summary, ACE and CEM are widely used the baseline HSI detectors. SRD is the most classic representation-learning-based HTD. hCEM is a famous hierarchical learning-based HSI target detector by suppressing undesired nontarget spectra while maintaining the key information of targets. SLRMDD and SSBRTD follow a similar detection paradigm to our proposed method by constructing or learning a unified background for detecting targets in HSI. Most of the source codes for these comparing methods are provided

Fig. 4. AVIRIS III hyperspectral data. *From left to right:* (a) Image scene. (b) Subimage scene. (c) Ground-truth of subimage scene.

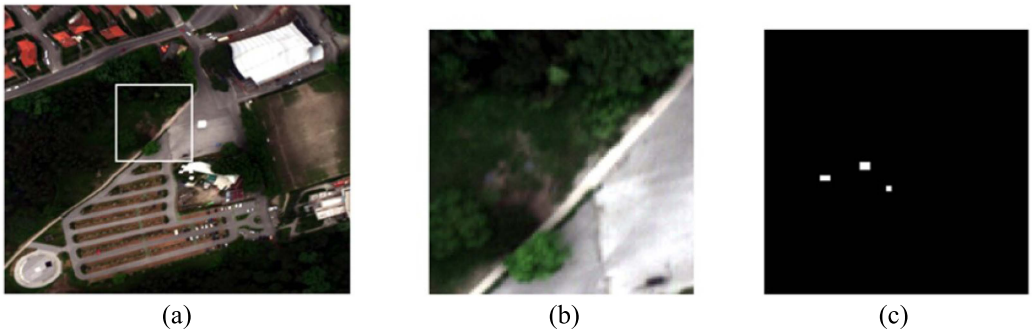

Fig. 5. Viareggio hyperspectral data. *From left to right:* (a) Image scene. (b) Subimage scene. (c) Ground-truth of subimage scene.

by the original authors and the key parameters therein are set as suggested by the authors.

C. Results and Analysis

This section will present the experimental results of different comparative methods on the four HSI target detection tasks from the perspectives of both qualitative and quantitative evaluations.

1) Qualitative Results: The detection maps of different methods on the four HSI datasets were plotted in Table II and compared with the ground-truth to evaluate the target detection performance of different methods qualitatively and intuitively, including the abilities of both target highlighting and background suppressing. Since the basic function of a target detector is to distinguish the target pixels from the observed HSI scene by suppressing the background pixels, an overall high-performance detector should generate a clear detection map, that is, it must highlight the target and, meanwhile, suppress the background component. According to the above-mentioned principles, some observations can be made from these results presented in Table II.

1) Most of the detection values in the detection maps produced by ACE are large, which might result in a high probability of target detection. However, the probability of a false alarm will also be high. Therefore, the results show that ACE has a higher target detection ability but lacks background suppression ability.
2) In contrast, CEM performs better in background suppression, but its target highlighting ability is fragile. Only a few of the target pixels can be detected and highlighted by CEM.
3) Comparatively speaking, the target and background pixels can be better distinguished and located by SRD, hCEM, SLRMDD, and SSBRTD. Among these four methods, SRD seems to perform better in highlighting targets. Nevertheless, the background suppression ability of SRD varies drastically from one dataset to another, which shows that the detection performance of SRD is not very stable.
4) The detection maps of hCEM, SLRMDD, and SSBRTD show better target highlighting ability, and the target location areas can be roughly observed in the obtained detection maps. However, their detection maps contain many pixels of detection value noise, which might lead to a higher probability of false alarms.

In comparison to the above-mentioned methods, the proposed TBMF detector can produce a more salient target detection map with fewer detection value noise pixels, and the target and background parts can be more clearly distinguished, especially at the edges of the target object, which indicates that the proposed TBMF detector performs efficiently in terms of both target highlighting and background suppression.

2) Quantitative Evaluation: Apart from the above qualitative assessments, some quantitative evaluation metrics were also used to evaluate different comparing methods, including the

TABLE II
VISUALIZATION FOR THE DETECTION MAPS OF DIFFERENT DETECTION METHODS

Tasks	ACE	CEM	SRD	hCEM	SLRMDD	SSBRTD	TBMF	Ground-truth
AVIRIS I		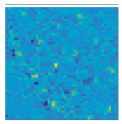	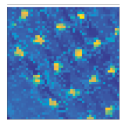	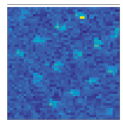	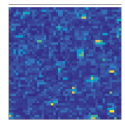	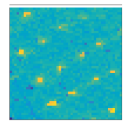	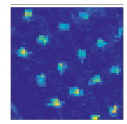	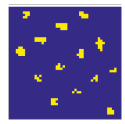
AVIRIS II		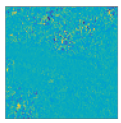	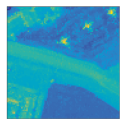	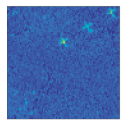	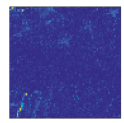		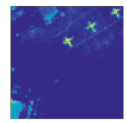	
AVIRIS III	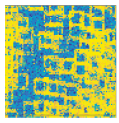	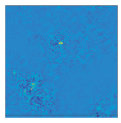	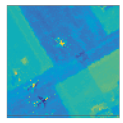	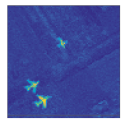	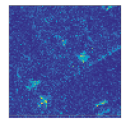	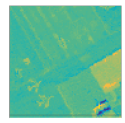	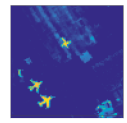	
Viareggio	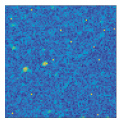	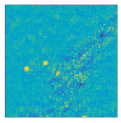	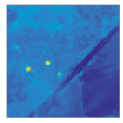	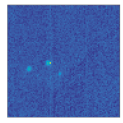	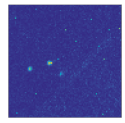	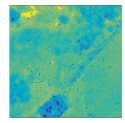	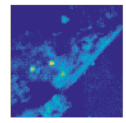	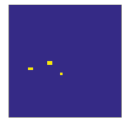

The horizontal and vertical coordinates in each plot indicate the spatial coordinates of the detection value for each HSI pixel.

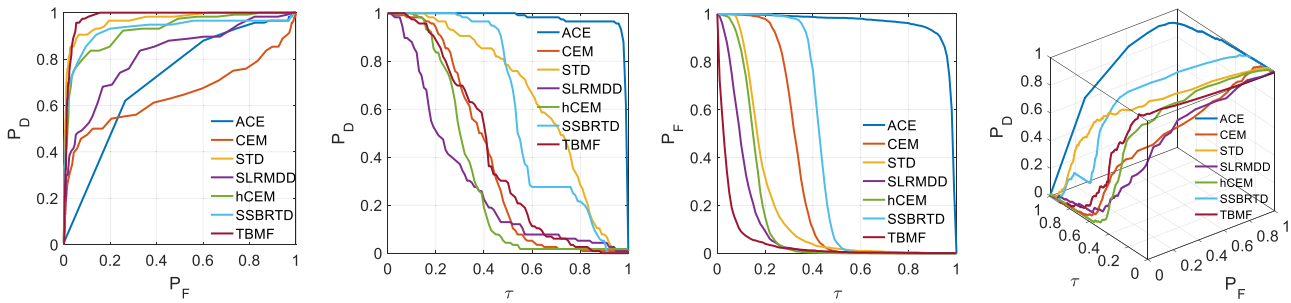

Fig. 6. Three kinds of 2-D ROC and the corresponding curves of different comparing methods on the AVIRIS I dataset. (a) ROC (PF, PD). (b) ROC $_{(\tau,\ \mathrm{PD})}$. (c) ROC $_{(\tau,\ \mathrm{PF})}$. (d) 3-D ROC curves.

TABLE III
AUC $_{(\mathrm{PF},\ \mathrm{PD})}$ VALUES OF DIFFERENT METHODS ON THE FOUR TASKS

Methods	Dataset			
	AVIRIS I	AVIRIS II	AVIRIS III	Viareggio
ACE	0.7529	0.6180	0.4417	0.9865
CEM	0.6442	0.6835	0.5385	0.9933
SRD	<u>0.9673</u>	0.9185	0.4305	**0.9998**
hCEM	0.9274	<u>0.9886</u>	**0.9980**	**0.9998**
SLRMDD	0.8199	0.9013	0.9087	0.9982
SSBRTD	0.9282	0.9203	0.7927	0.8208
TBMF	**0.9812**	**0.9985**	<u>0.9951</u>	<u>0.9997</u>

The best result is in bold and the second best is underlined.

TABLE IV
AUC $_{(\tau,\ \mathrm{PD})}$ VALUES OF DIFFERENT METHODS ON THE FOUR TASKS

Methods	Dataset			
	AVIRIS I	AVIRIS II	AVIRIS III	Viareggio
ACE	**0.9791**	0.9690	0.5653	0.6034
CEM	0.3865	0.4791	0.2917	**0.7950**
SRD	<u>0.6605</u>	0.6219	0.3693	<u>0.7146</u>
hCEM	0.3217	0.4087	0.4779	0.3882
SLRMDD	0.2859	0.1145	0.2966	0.4145
SSBRTD	0.6061	**0.7025**	<u>0.5893</u>	0.5860
TBMF	0.4080	<u>0.6449</u>	**0.6185**	0.6635

The best result is in bold and the second best is underlined.

three kinds of 2-D ROC curves, the 3-D ROC curve, as well as the corresponding AUC values for the three different 2-D ROC curves.

From the results presented in Figs. 6–9, and Tables III–V, one can see that the proposed TBMF method can achieve apparent superior results in comparison to the other methods in terms of the AUC$_{(\mathrm{PF},\ \mathrm{PD})}$ and AUC$_{(\tau,\ \mathrm{PF})}$, which shows that the

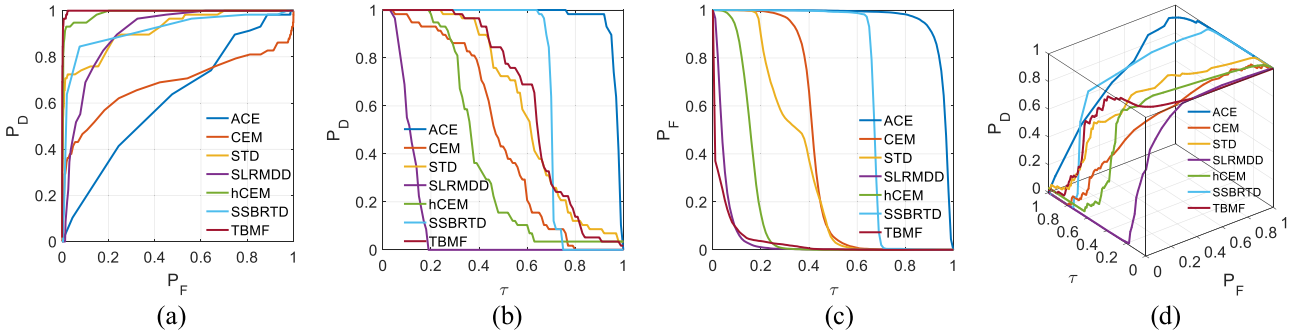

Fig. 7. Three kinds of 2-D ROC and the corresponding curves of different comparing methods on the AVIRIS II dataset. (a) ROC (PF, PD). (b) ROC (τ, PD). (c) ROC (τ, PF). (d) 3-D ROC curves.

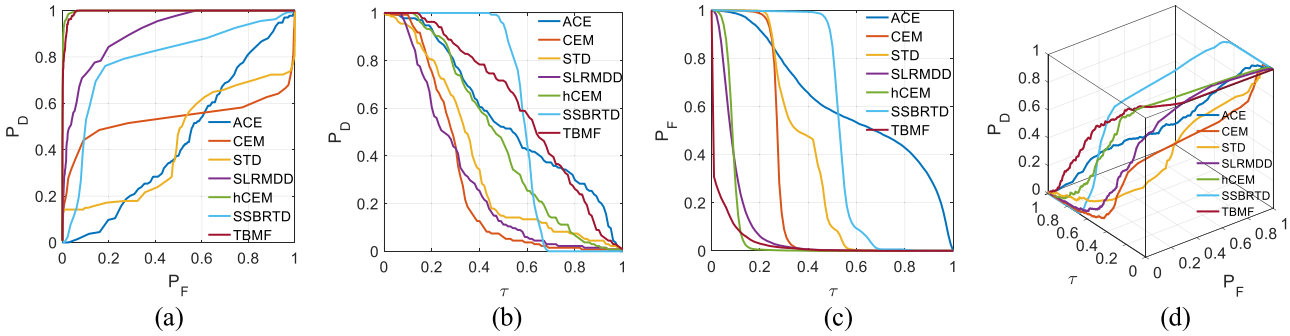

Fig. 8. Three kinds of 2-D ROC and the corresponding curves of different comparing methods on the AVIRIS III dataset. (a) ROC (PF, PD). (b) ROC (τ, PD). (c) ROC (τ, PF). (d) 3-D ROC curves.

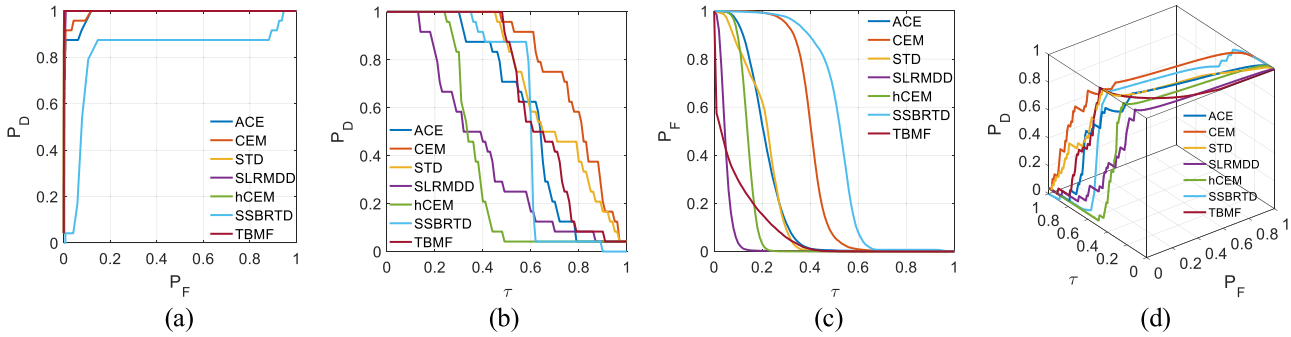

Fig. 9. Three kinds of 2-D ROC and the corresponding curves of different comparing methods on the Viareggio dataset. (a) ROC $(\mathrm{PF}, \mathrm{PD})$. (b) ROC (τ, PD). (c) ROC (τ, PF). (d) 3-D ROC curves.

proposed TBMF method has good target detection efficiency and background supersession ability. Although the comparing detectors, such as ACE and CEM, can achieve a higher AUC (τ, PD) than our proposed method on the AVIRIS I and Viareggio data, the AUC (τ, PF) for these comparing detectors also tend to be high, which means that their background suppression ability is insufficient.

In fact, it is challenging for a detector to simultaneously yield the highest AUC (τ, PD) as well as the lowest AUC (τ, PF). A good detector should strike a balance between target highlighting ability and background suppressing ability, i.e., higher AUC (τ, PD) and lower AUC (τ, PF).

Recent studies show that any individual AUC value cannot truly and objectively evaluate the detection performance of different methods. When comprehensively considering the three AUC values based on $\mathrm{AUC}_{(\mathrm{PF,PD})}$, $\mathrm{AUC}_{(\tau,\mathrm{PD})}$, and $\mathrm{AUC}_{(\tau,\mathrm{PF})}$, using $\mathrm{AUC}_{\mathrm{OA}}$ and $\mathrm{AUC}_{\mathrm{SNPR}}$, our proposed TBMF method can generally yield superior performance.

Concretely, as given in Table VI, the proposed TBMF method can achieve the highest $\mathrm{AUC}_{\mathrm{OA}}$ value on the AVIRIS II, AVIRIS III, and Viareggio datasets. The performance improvements are 29.85% (1.2404→1.6107), 14.02% (1.3886→1.5834), and 4.97% (1.5088→1.5838), when compared with the second-best results achieved by hCEM and SRD. As for the AVIRIS I

TABLE V
AUC $_{(\tau,\ \mathrm{PF})}$ VALUES OF DIFFERENT METHODS ON THE FOUR TASKS

Methods	Dataset			
	AVIRIS I	AVIRIS II	AVIRIS III	Viareggio
ACE	0.9578	0.9543	0.6217	0.2122
CEM	0.3244	0.4147	0.2720	0.4046
SRD	0.1910	0.3376	0.3711	0.2056
hCEM	0.1521	0.1569	0.0874	0.1389
SLRMDD	0.1084	0.0482	0.0948	**0.0488**
SSBRTD	0.4271	0.6697	0.5364	0.5108
TBMF	**0.0462**	**0.0327**	**0.0302**	0.0794

The best result is in bold and the second best is underlined.

TABLE VI
AUC$_{\mathrm{OA}}$ VALUES OF DIFFERENT METHODS ON THE FOUR TASKS

Methods	Dataset			
	AVIRIS I	AVIRIS II	AVIRIS III	Viareggio
ACE	0.7742	0.6327	0.3854	1.3778
CEM	0.7063	0.7479	0.5582	1.3837
SRD	**1.4368**	1.2028	0.4287	1.5088
hCEM	1.0970	1.2404	1.3886	1.2491
SLRMDD	0.9974	0.9676	1.1105	1.3639
SSBRTD	1.1072	0.9531	0.8456	0.8960
TBMF	1.3430	**1.6107**	**1.5834**	**1.5838**

The best result is in bold and the second best is underlined.

TABLE VII
AUC$_{\mathrm{SNPR}}$ VALUES OF DIFFERENT METHODS ON THE FOUR TASKS

Methods	Dataset			
	AVIRIS I	AVIRIS II	AVIRIS III	Viareggio
ACE	1.0222	1.0154	0.9094	2.8443
CEM	1.1914	1.1553	1.0724	1.9650
SRD	3.4581	1.8421	0.9950	3.4756
hCEM	2.1151	2.6048	5.4703	2.7943
SLRMDD	2.6375	2.3755	3.1271	**8.4922**
SSBRTD	1.4191	1.0490	1.0987	1.1471
TBMF	**8.8352**	**19.7217**	**20.4970**	8.3558

The best result is in bold and the second best is underlined.

data, the AUC$_{\mathrm{OA}}$ value of the proposed TBMF method is in second place, which is slightly lower than that of SRD with a degradation of about 7% (1.3427→1.4368). Similarly, our TBMF method can yield the highest AUC$_{\mathrm{SNPR}}$ values on the AVIRIS I, AVIRIS II, and AVIRIS III datasets as shown in Table VII, and the gains of our method than the second-best results are about 155.49% (3.4581→8.8352), 657.13% (2.6048→19.7219), and 274.70% (5.4703→20.4970), respectively.

As a result, the proposed TBMF method shows promising performance when evaluating the different methods using the two overall AUC values, i.e., AUC$_{\mathrm{OA}}$ and AUC$_{\mathrm{SNPR}}$, and yields comprehensive target detection and background suppression benefits when compared with some other state-of-the-art methods.

TABLE VIII
AUC$_{\mathrm{OA}}$ VALUE COMPARISON FOR THE FOUR DATASETS WITH GAUSSIAN AND STRIPES NOISE POLLUTED

Methods	Dataset			
	AVIRIS I	AVIRIS II	AVIRIS III	Viareggio
ACE	0.9179	0.6834	0.5796	0.7474
CEM	0.2517	0.8362	0.6154	1.2494
SRD	0.3117	1.1498	0.5863	1.0172
hCEM	0.8710	1.4942	1.0705	1.3435
SLRMDD	0.6598	1.2549	1.2272	1.1569
SSBRTD	0.4380	0.6966	0.4195	0.3055
TBMF	**1.2531**	**1.6114**	**1.4025**	**1.5769**

The best result is shown in bold and the second-best result is underlined.

TABLE IX
AUC$_{\mathrm{SNPR}}$ VALUE OF COMPARISON FOR THE FOUR DATASETS WITH GAUSSIAN AND STRIPES NOISE POLLUTED

Methods	Dataset			
	AVIRIS I	AVIRIS II	AVIRIS III	Viareggio
ACE	1.4440	1.3674	1.0091	1.0078
CEM	0.9145	1.2578	1.1105	1.6275
SRD	0.7314	1.8699	1.0537	1.4523
hCEM	1.3136	3.7627	1.4212	2.5355
SLRMDD	1.3663	13.2297	**25.7680**	1.9037
SSBRTD	0.9612	1.1353	0.9480	0.8130
TBMF	**4.5117**	**18.1136**	15.2515	**10.7348**

The best result is shown in bold and the second-best result is underlined.

D. Discussion

1) Experiments With Noisy Data: For a real-world HSI target detection task, the collected HSI data are always corrupted by noise from both internal sensors and the external observation environment, which will introduce complex nontarget nonbackground noise interference information contained in the HSI data, and bring great challenge to the accurate detection of targets. As a result, an HSI target detector should deal with the complex noise and reduce its negative impact on the detection performance. Thus, the proposed TBMF method proposes to precisely model the target component, background component, and nontarget nonbackground noise component. This section will study the noise-robust properties of different methods. In the experiments, the noisy HSI datasets containing Gaussian and stripes noise corresponding to the AVIRIS I, AVIRIS II, AVIRIS III, and Viareggio datasets are simulated. The Gaussian noise elements $\mathbf{n} \sim \mathcal{N}(0,\ (\mathbf{Dm})^2)$, where $\mathbf{Dm}$ is a diagonal matrix with diagonal sampled from a uniform distribution $\mathrm{U}(0,\ 0.01)$. In addition, the oblique stripe noise randomly affects 30% of the bands and then leads to the final noisy HSI data, as shown in Fig. 10. The overall AUC$_{\mathrm{OA}}$ and AUC$_{\mathrm{SNPR}}$ performance of different methods on the noisy HSI dataset is reported in Tables VIII and IX. The results show that, in comparison to the other methods, the proposed method can consistently yield promising performance when the data are severely polluted by complex mixed noise. The results verify that the $l_{1,1}$-norm-based noise regularization introduced in the proposed method can better characterize the complex distribution of noise than the other noise regularization, such as the Frobenius norm-based noise

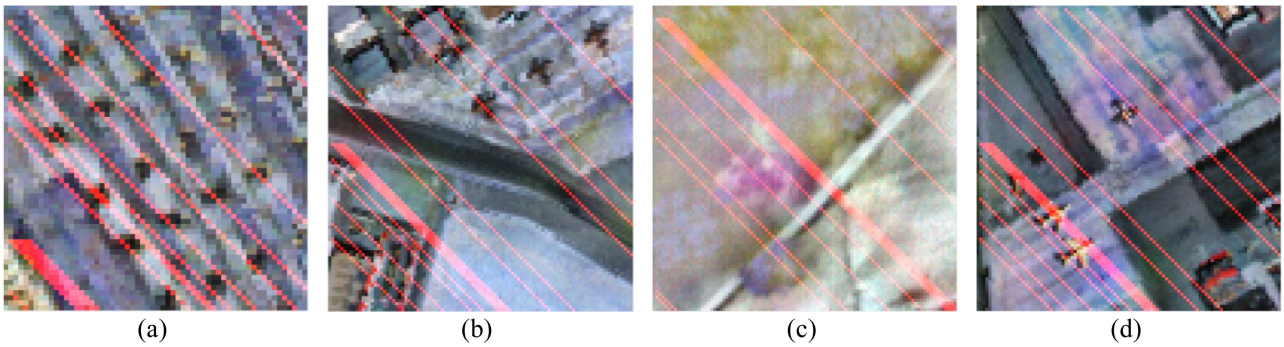

Fig. 10. Gaussian and stripes noise polluted HSI data. (a) AVIRIS I. (b) AVIRIS II. (c) AVIRIS III. (d) Viareggio.

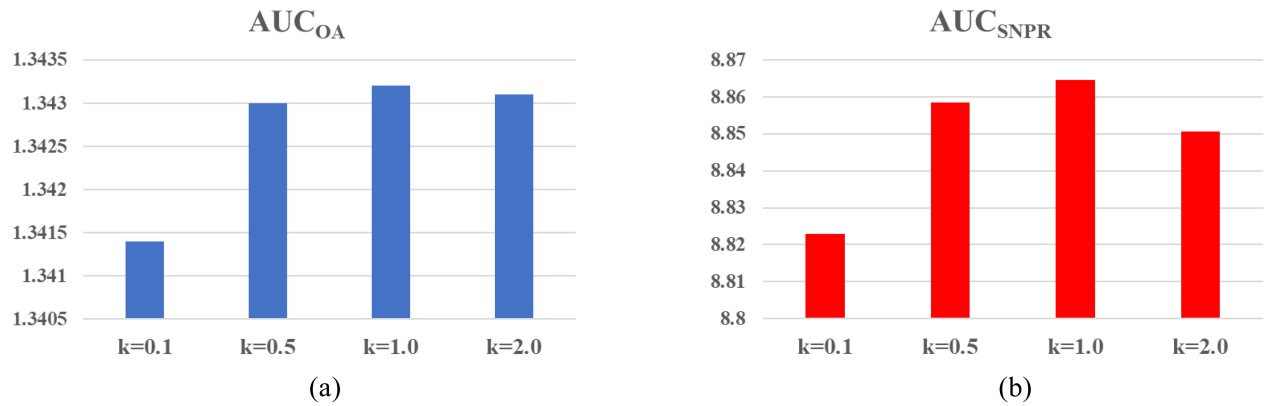

Fig. 11. $\mathrm{AUC_{OA}}$ and $\mathrm{AUC_{SNPR}}$ values of the proposed detector with different k on the AVIRIS I dataset. (a) $\mathrm{AUC_{OA}}$. (b) $\mathrm{AUC_{SNPR}}$.

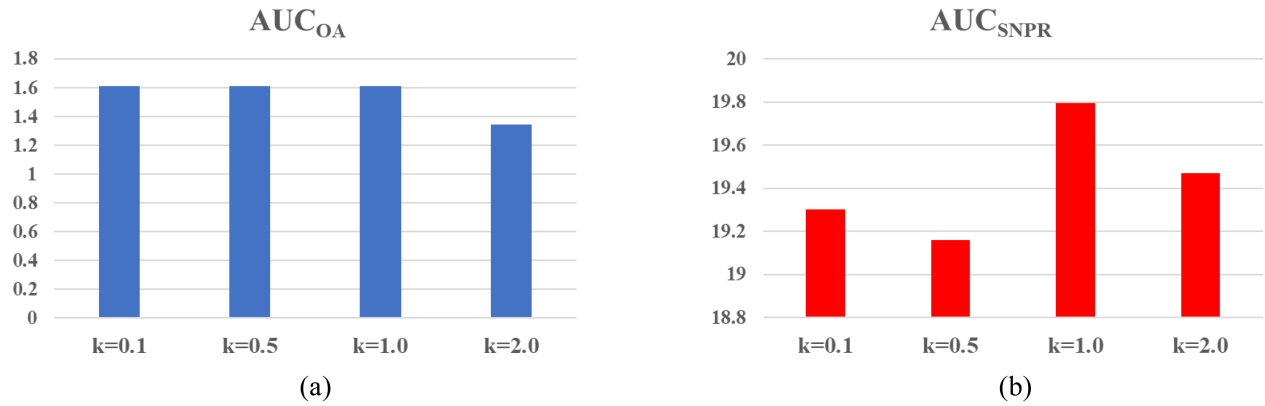

Fig. 12. $\mathrm{AUC_{OA}}$ and $\mathrm{AUC_{SNPR}}$ values of the proposed detector with different k on the AVIRIS II dataset. (a) $\mathrm{AUC_{OA}}$. (b) $\mathrm{AUC_{SNPR}}$.

regularization adopted in the SLRMDD method. As a result, the noise in HSI data can be accurately removed with our method, and thus, more accurate target and background components can be separated to achieve stable detection performance.

2) Parameters Analysis: The proposed TBMF method proposes to introduce a learnable target spectra dictionary $\mathbf{B} \in \Re^{p \times n_2}$ containing n_2 atoms to augment the limited available target prior spectra and appropriately embed them into the HSI data decomposition model. With the idea, in the experiments, considerable target prior spectra can be generated and augmented through our model to guide the accurate separation of background components from HSI data. Empirically, the pixel number of the augmented target spectra dictionary n_2 can be manually set and is usually larger than the number of the original available prior target prior spectra n_1. For simplicity, n_2 can be set around the number of spectral bands p as $k \cdot p$ with $k = 0.1, 0.5, 1.0, 2.0$, wherein k is the spectral augmentation index. Figs. 11 and 12 show the influences of k on the detection

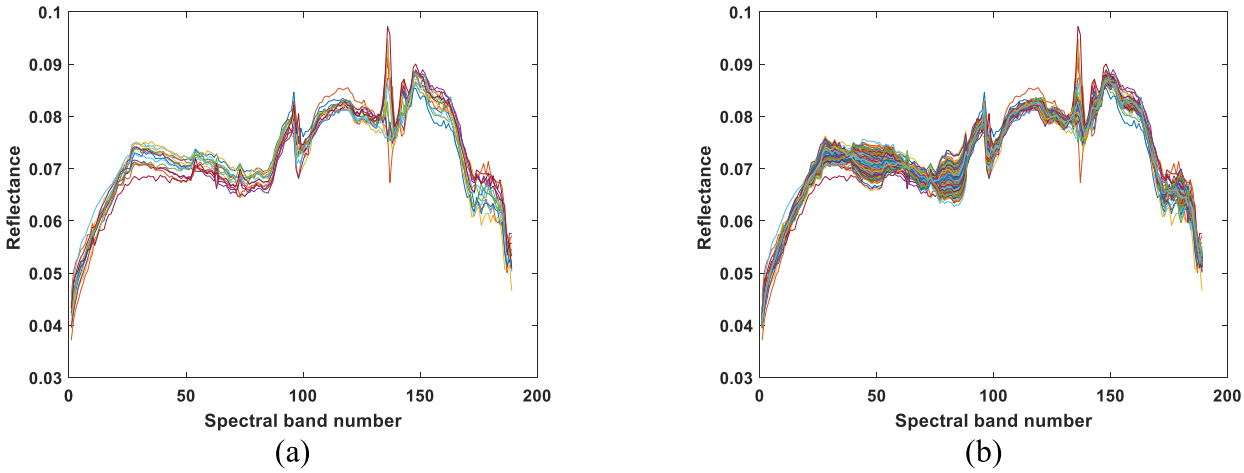

Fig. 13. Target prior spectra augmentation ability of our proposed method when $k = 1$ on the AVIRIS I dataset. (a) Original available target prior spectra. (b) Augmented target prior spectra simultaneously generated by our method.

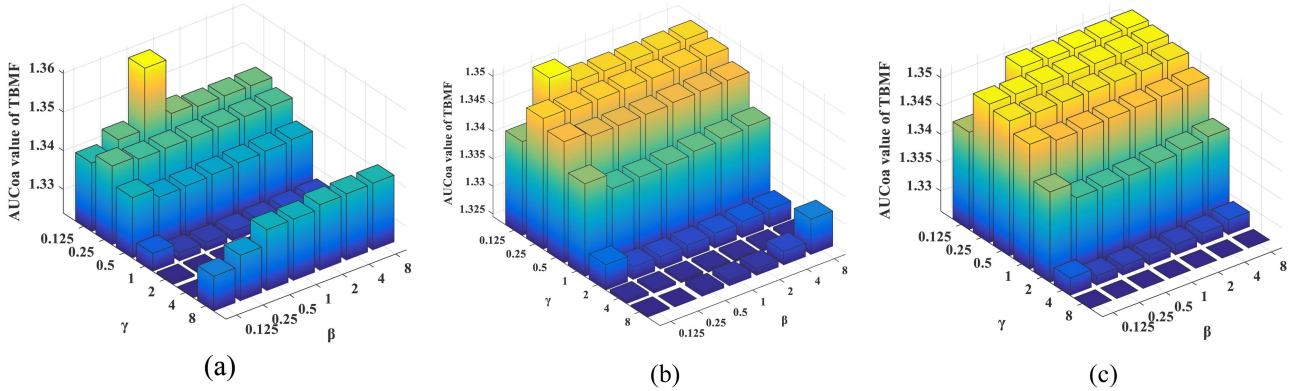

Fig. 14. Performance of TBMF with respect to different settings of parameter α with β and γ changing in the candidate parameter set $\{2^{-3}, 2^{-2}, 2^{-1}, 2^0, 2^1, 2^2, 2^3\}$ on the AVIRIS I dataset. (a) $\alpha = 0.5$. (b) $\alpha = 1$. (c) $\alpha = 2$.

performance reflected by $\mathrm{AUC_{OA}}$ and $\mathrm{AUC_{SNPR}}$ on the AVIRIS I and AVIRIS II datasets, respectively.

When the parameter k is low ($= 0.1, 0.5$), the detection performance on the testing datasets is unsatisfactory, the possible reason for this is that a lower k can only generate less target prior spectra through the embed-constrained linear spectral mixture model. When k increases, more diverged target prior spectra can be generated to supervise the separation of the pure background component, and thus, the proposed method tends to achieve improved detection performance. However, when k is too large, some redundant and interference information will be introduced, which may degrade the detection performance. Therefore, in the experiments, the parameter k can be empirically set to 1, i.e., $n_2 = p$, and the number of the newly augmented target prior spectra is equal to the number of spectral bands. Fig. 13 illustrates a case for the target prior spectra augmentation ability of our proposed method on the AVIRIS I dataset. In comparison to the original available target prior spectra, embed-constrained linear spectral mixture model can generate considerable target prior spectra, which share a similar spectral curve with the original available target prior spectra, and provide more supervision information for HSI data decomposition and the subsequent target detection.

In addition, there are three parameters α, β, and γ in the objective function (8), which can balance the corresponding modules in the optimization objective model. Empirically, different settings of these parameters will influence the convergence property and performance of the optimization algorithms and then lead to different detection performances of the TBMF method.

For parameter setting, it is reasonable to assume that the three components weighted by α, β, and γ play equally important roles in the optimization problem, that is, α, β, and γ can take value around 1. As a result, for simplicity, the three parameters can be empirically adjusted from the candidate parameter set $\{2^{-3}, 2^{-2}, 2^{-1}, 2^0, 2^1, 2^2, 2^3\}$. Fig. 14 shows the detection performance variations of the TBMF method with respect to different settings of parameter α, when β and γ change in the set $\{2^{-3}, 2^{-2}, 2^{-1}, 2^0, 2^1, 2^2, 2^3\}$ on the AVIRIS I dataset. The figure shows that the detection performance of our TBMF method varies significantly under different settings of α, β, and γ. When $\alpha < 1$, the detection performance of our TBMF method seems to

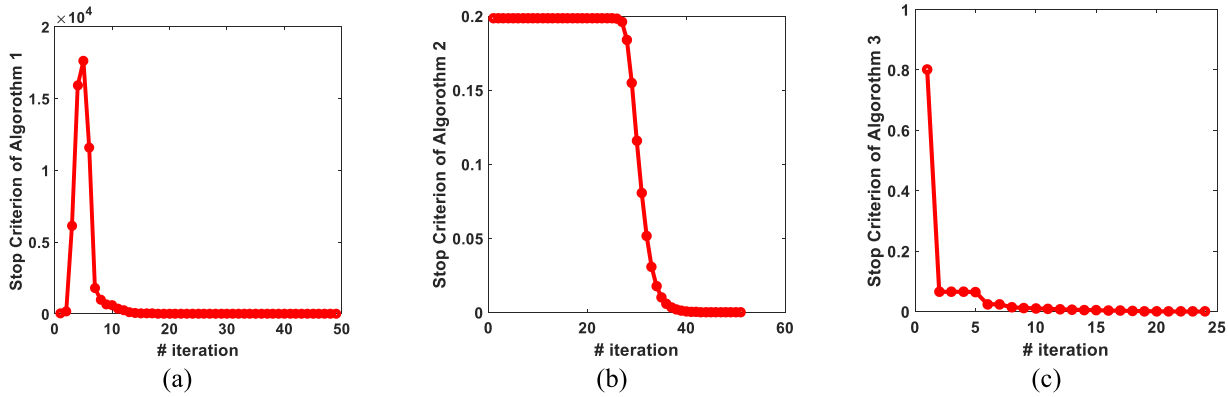

Fig. 15. Iteration stop criterion variations of the three optimization algorithms on the AVIRIS I dataset with proper balancing parameter settings. (a) Algorithm 1. (b) Algorithm 2. (3) Algorithm 3.

be inferior, even when the settings of β and γ are set with the grid-search strategy. By comparison, when $\alpha \geq 1$, the performance of TBMF tends to be more stable and better when β and γ vary in the whole parameter candidate range. Specifically, when $\gamma \in (2^{-3}, 1)$ and $\beta \in (1, 8)$, more stable and promising detection performance can be achieved by our proposed TBMF method. Similar results can be observed in the other datasets. Therefore, it is recommended to adjust the settings of the three parameters to around 1, according to different specific detection tasks.

In addition to the detection performance, proper settings of the balancing parameters will also influence the convergence property of the devised Algorithms 1–3. Fig. 15 shows the iteration stop criterion value variations for the stop criteria in the three optimization algorithms on the AVIRIS I dataset. The three optimization algorithms can converge quickly within 50 iterations, which demonstrates the efficiency of the devised three optimization algorithms with proper parameters.

V. Conclusion

This article has presented a novel TBMF method for target detection in HSI. The method focuses on the dilemmas of HTD, including pure background spectra separation, insufficient target prior spectra, and data noise pollution. Concretely, the method proposes to learn adequate and high-quality target and background spectra and then highlight the target component by suppressing the background component for accurate detection of target pixels in HSI. To achieve this, a unified HSI data decomposition model is formulated for diverse target prior spectra augmentation, pure background spectra separation, and complex nontarget nonbackground noise removal. Furthermore, a group of basic CEM detectors is trained in parallel in a background-suppressed subspace induced by the separated pure background component. The detection results achieved by these basic detectors are fused to take full advantage of all the augmented diverse target prior spectra. Experimental results on several benchmark HSI target detection datasets show that the proposed TBMF method can yield promising detection performance when compared with several state-of-the-art detection methods even when the HSI data are severely polluted with complex noise.

References

[1] F. Luo, T. Zhou, J. Liu, T. Guo, X. Gong, and J. Ren, "Multiscale diff-changed feature fusion network for hyperspectral image change detection," *IEEE Trans. Geosci. Remote Sens.*, vol. 61, 2023, Art. no. 5502713.

[2] T. Guo, R. Wang, F. Luo, X. Gong, L. Zhang, and X. Gao, "Dual-view spectral and global spatial feature fusion network for hyperspectral image classification," *IEEE Trans. Geosci. Remote Sens.*, vol. 61, 2023, Art. no. 5512913.

[3] Y. Duan, F. Luo, M. Fu, Y. Niu, and X. Gong, "Classification via structure-preserved hypergraph convolution network for hyperspectral image," *IEEE Trans. Geosci. Remote Sens.*, vol. 61, 2023, Art. no. 5507113.

[4] T. Guo, L. He, F. Luo, X. Gong, Y. Li, and L. Zhang, "Anomaly detection of hyperspectral image with hierarchical anti-noise mutual-incoherence-induced low-rank representation," *IEEE Trans. Geosci. Remote Sens.*, vol. 61, 2023, Art. no. 5510213.

[5] T. Guo, F. Luo, L. Zhang, B. Zhang, X. Tan, and X. Zhou, "Learning structurally incoherent background and target dictionaries for hyperspectral target detection," *IEEE J. Sel. Topics Appl. Earth Observ. Remote Sens.*, vol. 13, pp. 3521–3533, 2020.

[6] X. Yang, B. Tu, Q. Li, J. Li, and A. Plaza, "Graph evolution-based vertex extraction for hyperspectral anomaly detection," *IEEE Trans. Neural Netw. Learn. Syst.*, to be published, doi: 10.1109/TNNLS.2023.3303273.

[7] X. Liao, B. Tu, J. Li, and A. Plaza, "Class-wise graph embedding-based active learning for hyperspectral image classification," *IEEE Trans. Geosci. Remote Sens.*, vol. 61, 2023, Art. no. 5522813, doi: 10.1109/TGRS.2023.3309032.

[8] B. Tu, W. He, Q. Li, Y. Peng, and A. Plaza, "A new context-aware framework for defending against adversarial attacks in hyperspectral image classification," *IEEE Trans. Geosci. Remote Sens.*, vol. 61, 2023, Art. no. 5505114.

[9] Y. Niu and B. Wang, "Extracting target spectrum for hyperspectral target detection: An adaptive weighted learning method using a self-completed background dictionary," *IEEE Trans. Geosci. Remote Sens.*, vol. 55, no. 3, pp. 1604–1617, Mar. 2017.

[10] S. Yang and Z. Shi, "SparseCEM and SparseACE for hyperspectral image target detection," *IEEE Geosci. Remote Sens. Lett.*, vol. 11, no. 12, pp. 2135–2139, Dec. 2014.

[11] H. Zhuang, K. Deng, H. Fan, and M. Yu, "Strategies combining spectral angle mapper and change vector analysis to unsupervised change detection in multispectral images," *IEEE Geosci. Remote Sens. Lett.*, vol. 13, no. 5, pp. 681–685, May 2016.

[12] H. Kwon and N. M. Nasrabadi, "Kernel adaptive subspace detector for hyperspectral imagery," *IEEE Geosci. Remote Sens. Lett.*, vol. 3, no. 2, pp. 271–275, Apr. 2006.

[13] H.-C. Li, C.-I. Chang, and M. Song, "Recursive band processing of orthogonal subspace projection for hyperspectral imagery," *IEEE Geosci. Remote Sens. Lett.*, vol. 13, no. 1, pp. 3–7, Jan. 2016.

[14] X. Shang, M. Song, and C.-I. Chang, "An iterative random training sample selection approach to constrained energy minimization for hyperspectral image classification," *IEEE Geosci. Remote Sens. Lett.*, vol. 18, no. 9, pp. 1625–1629, Sep. 2021.

[15] X. Shang et al., "Target-constrained interference-minimized band selection for hyperspectral target detection," *IEEE Trans. Geosci. Remote Sens.*, vol. 59, no. 7, pp. 6044–6064, Jul. 2021.
[16] D. Zhu, B. Du, and L. Zhang, "Target dictionary construction-based sparse representation hyperspectral target detection methods," *IEEE J. Sel. Topics Appl. Earth Observ. Remote Sens.*, vol. 12, no. 4, pp. 1254–1264, Apr. 2019.
[17] D. Zhu, B. Du, and L. Zhang, "Single-spectrum-driven binary-class sparse representation target detector for hyperspectral imagery," *IEEE Trans. Geosci. Remote Sens.*, vol. 59, no. 2, pp. 1487–1500, Feb. 2021.
[18] S. Zhang et al., "Spectral-spatial hyperspectral unmixing using nonnegative matrix factorization," *IEEE Trans. Geosci. Remote Sens.*, vol. 60, 2022, Art. no. 5505713.
[19] A. W. Bitar, L.-F. Cheong, and J.-P. Ovarlez, "Sparse and low-rank matrix decomposition for automatic target detection in hyperspectral imagery," *IEEE Trans. Geosci. Remote Sens.*, vol. 57, no. 8, pp. 5239–5251, Aug. 2019.
[20] Y. Chen, N. M. Nasrabadi, and T. D. Tran, "Sparse representation for target detection in hyperspectral imagery," *IEEE J. Sel. Topics Signal Process.*, vol. 5, no. 3, pp. 629–640, Jun. 2011.
[21] Y. Zhang, B. Du, and L. Zhang, "A sparse representation-based binary hypothesis model for target detection in hyperspectral images," *IEEE Trans. Geosci. Remote Sens.*, vol. 53, no. 3, pp. 1346–1354, Mar. 2015.
[22] W. Li, Q. Du, and B. Zhang, "Combined sparse and collaborative representation for hyperspectral target detection," *Pattern Recognit.*, vol. 48, no. 12, pp. 3904–3916, 2015.
[23] T. Guo, F. Luo, L. Zhang, X. Tan, J. Liu, and X. Zhou, "Target detection in hyperspectral imagery via sparse and dense hybrid representation," *IEEE Geosci. Remote Sens. Lett.*, vol. 17, no. 4, pp. 716–720, Apr. 2020.
[24] Z. Zou and Z. Shi, "Hierarchical suppression method for hyperspectral target detection," *IEEE Trans. Geosci. Remote Sens.*, vol. 54, no. 1, pp. 330–342, Jan. 2016.
[25] D. Zhu, B. Du, and L. Zhang, "Two-stream convolutional networks for hyperspectral target detection," *IEEE Trans. Geosci. Remote Sens.*, vol. 59, no. 8, pp. 6907–6921, Aug. 2021.
[26] G. Zhang, S. Zhao, W. Li, Q. Du, Q. Ran, and R. Tao, "HTD-Net: A deep convolutional neural network for target detection in hyperspectral imagery," *Remote Sens.*, vol. 12, no. 9, 2020, Art. no. 1489.
[27] E. Cands, X. Li, Y. Ma, and J. Wright, "Robust principal component analysis?," *J. Assoc. Comput. Mach.*, vol. 58, no. 3, pp. 1–37, 2009.
[28] G. Liu, Z. Lin, S. Yan, J. Sun, Y. Yu, and Y. Ma, "Robust recovery of subspace structures by low-rank representation," *IEEE Trans. Pattern Anal. Mach. Intell.*, vol. 35, no. 1, pp. 171–184, Jan. 2013.
[29] E. Elhamifar and R. Vidal, "Sparse subspace clustering: Algorithm, theory, and applications," *IEEE Trans. Pattern Anal. Mach. Intell.*, vol. 35, no. 11, pp. 2765–2781, Nov. 2013.
[30] Z. Lin, R. Liu, and Z. Su, "Linearized alternating direction method with adaptive penalty for low-rank representation," in *Proc. Adv. Neural Inform. Process. Syst.*, vol. 2011, pp. 612–620, 2011.
[31] C.-I. Chang, "An effective evaluation tool for hyperspectral target detection: 3D receiver operating characteristic curve analysis," *IEEE Trans. Geosci. Remote Sens.*, vol. 59, no. 6, pp. 5131–5153, Jun. 2021.
[32] B. Tu, X. Liao, Q. Li, Y. Peng, and A. Plaza, "Local semantic feature aggregation-based transformer for hyperspectral image classification," *IEEE Trans. Geosci. Remote Sens.*, vol. 60, 2022, Art. no. 5536115.
[33] T. Guo, X.-P. Lu, K. Yu, Y.-X. Zhang, and W. Wei, "Integration of light curve brightness information and layered discriminative constrained energy minimization for automatic binary asteroid detection," *IEEE Trans. Aerosp. Electron. Syst.*, vol. 58, no. 6, pp. 4984–4999, Dec. 2022.
[34] B. Tu, Q. Ren, Q. Li, W. He, and W. He, "Hyperspectral image classification using a superpixel-pixel-subpixel multilevel network," *IEEE Trans. Instrum. Meas.*, vol. 72, 2023, Art. no. 5013616.
[35] X. Wang, L. Wang, Q. Wang, A. Vizziello, and P. Gamba, "Hyperspectral target detection via global spatial-spectral attention network and background suppression," *IEEE J. Sel. Topics Appl. Earth Observ. Remote Sens.*, vol. 16, pp. 9011–9024, 2023, doi: 10.1109/JSTARS.2023.3310189.
[36] J. Jiao, Z. Gong, and P. Zhong, "Triplet spectralwise transformer network for hyperspectral target detection," *IEEE Trans. Geosci. Remote Sens.*, vol. 61, 2023, Art. no. 5519817.
[37] D. Shen, X. Ma, W. Kong, J. Liu, J. Wang, and H. Wang, "Hyperspectral target detection based on interpretable representation network," *IEEE Trans. Geosci. Remote Sens.*, vol. 61, 2023, Art. no. 5519416.
[38] Y. Gao et al., "Hyperspectral and multispectral classification for coastal wetland using depthwise feature interaction network," *IEEE Trans. Geosci. Remote Sens.*, vol. 60, 2022, Art. no. 5512615.
[39] S. Li, W. Song, L. Fang, Y. Chen, P. Ghamisi, and J. A. Benediktsson, "Deep learning for hyperspectral image classification: An overview," *IEEE Trans. Geosci. Remote Sens.*, vol. 57, no. 9, pp. 6690–6709, Sep. 2019.
[40] W. Song, Y. Dai, Z. Gao, L. Fang, and Y. Zhang, "Hashing-based deep metric learning for the classification of hyperspectral and LiDAR data," *IEEE Trans. Geosci. Remote Sens.*, vol. 61, 2023, Art. no. 5704513.
[41] W. Song, S. Li, L. Fang, and T. Lu, "Hyperspectral image classification with deep feature fusion network," *IEEE Trans. Geosci. Remote Sens.*, vol. 56, no. 6, pp. 3173–3184, Jun. 2018.